environmental microbiology

Environmental Microbiology (2017) **19**(11), 4417–4431 doi:10.1111/1462-2920.13883

Fluid-driven interfacial instabilities and turbulence in bacterial biofilms

Stefania Fabbri,[1] Jian Li,[2] Robert P. Howlin,[3,4] Amir Rmaile,[5] Bart Gottenbos,[5] Marko De Jager,[5] E. Michelle Starke,[6] Marcelo Aspiras,[7] Marilyn T. Ward,[6] Nicholas G. Cogan[2] and Paul Stoodley[1,8*]

[1]*National Centre for Advanced Tribology at Southampton (nCATS), Mechanical Engineering Department, University of Southampton, Southampton SO17 1BJ, UK.*

[2]*Department of Mathematics, Florida State University, Tallahassee, FL 32306, USA.*

[3]*National Institute for Health Research Southampton Respiratory Biomedical Research Unit, Southampton Centre for Biomedical Research, University Hospital Southampton NHS Foundation Trust, Southampton SO17 1BJ, UK.*

[4]*Centre for Biological Sciences, Faculty of Natural and Environmental Sciences and Institute for Life Sciences, University of Southampton, Southampton SO17 1BJ, UK.*

[5]*Philips Research, Eindhoven 5656 AE, The Netherlands.*

[6]*Philips Oral Healthcare, Bothell, Washington 98021, USA.*

[7]*Wrigley-MARS, Chicago, IL 60613, USA.*

[8]*Department of Microbial Infection and Immunity and the Department of Orthopaedics, Centre for Microbial Interface Biology, The Ohio State University, Columbus, OH, 43210, USA..*

Summary

Biofilms are thin layers of bacteria embedded within a slime matrix that live on surfaces. They are ubiquitous in nature and responsible for many medical and dental infections, industrial fouling and are also evident in ancient fossils. A biofilm structure is shaped by growth, detachment and response to mechanical forces acting on them. The main contribution to biofilm versatility in response to physical forces is the matrix that provides a platform for the bacteria to grow. The interaction between biofilm structure and hydrodynamics remains a fundamental question concerning biofilm dynamics. Here, we document the appearance of ripples and wrinkles in biofilms grown from three species of bacteria when subjected to high-velocity fluid flows. Linear stability analysis suggested that the ripples were Kelvin–Helmholtz Instabilities. The analysis also predicted a strong dependence of the instability formation on biofilm viscosity explaining the different surface corrugations observed. Turbulence through Kelvin–Helmholtz instabilities occurring at the interface demonstrated that the biofilm flows like a viscous liquid under high flow velocities applied within milliseconds. Biofilm fluid-like behavior may have important implications for our understanding of how fluid flow influences biofilm biology since turbulence will likely disrupt metabolite and signal gradients as well as community stratification.

Introduction

Biofilms are surface-attached microbial communities surrounded by a self-produced matrix of extracellular polymeric substances (EPS), which include polysaccharides, proteins, lipids and nucleic acids (Hanks and Ruo, 1966; Flemming and Wingender, 2010). Biofilms are ubiquitous in the natural environment and have been identified in the fossil record (Stoodley *et al.*, 2002a). Biofilms colonize all man-made surfaces such as ship hulls, industrial pipelines and biomedical implants, as well as human tissues and oral surfaces (Costerton *et al.*, 1999; Marsh, 2004; Schultz *et al.*, 2011). A common feature of these surfaces is that they are in contact with fluid flow. The hydrodynamic flow is known to affect biofilm formation, behaviour, structure and propagation. Biofilms are not static but are highly dynamic with their structure shaped by growth, detachment and response to mechanical forces acting on them (Stewart, 2014). The EPS network provides the main source of biofilm versatility in response to physical forces and also endows the biofilm with non-trivial mechanical properties (Fabbri and Stoodley, 2016).

Received 11 February, 2017; accepted 3 August, 2017. *For correspondence. E-mail Paul.stoodley@osumc.edu; Tel. +1 614 292 7826; Fax. +1 614 292 9616.

Biofilms are widely acknowledged to be viscoelastic materials (Wilking *et al*., 2011; Billings *et al*., 2015; Peterson *et al*., 2015; Fabbri and Stoodley, 2016). As with all viscoelastic materials, they can be dominated by an elastic response, a viscous response or a viscoelastic response depending on (1) the magnitude of the imposed load, (2) the time scale over which the load is imposed and (3) the rate at which the load is imposed. The same biofilm can behave like a fluid under certain conditions, a solid under others, and a mixture of the two under others. In addition, biofilms can change their shape through growth and detachment process to adapt their life under different fluid flows conditions (Böl *et al*., 2009; Blauert *et al*., 2015). Flow cell experiments have shown that biofilms can structurally reorganize in response to elevated shear to form drag reducing forms such as streamers or ripples over days (Stoodley *et al*., 1999c). Wave-like pattern biofilms have also been found inside endotracheal tubes (Inglis, 1993) and venous catheters (Rusconi *et al*., 2010). Biofilm rippling has also been related to the large pressure drops and drag associated with biofilms in systems ranging from industrial pipelines (Lappin-Scott and Costerton, 1989) to ship hulls (Schultz *et al*., 2011). Similar structures have been observed in the natural environment, ranging from modern biofilms grown under high-velocity flows in *in vitro* streamside (Stoodley *et al*., 1999b; Battin *et al*., 2003) to ancient microbially induced sedimentary structures (MISS) (Noffke *et al*., 2001; Porada *et al*., 2008). Whether the interaction between biofilms and hydrodynamic forces is an adaptation of biofilms as multicellular entities to withstand shear forces still remains a fundamental research question (Drescher *et al*., 2013). Recent studies have raised the hypothesis that ripple structures formed in ancient fossils may be the result of Kelvin–Helmholtz Instabilities (KHI) which occur between the microbial biofilm and the overlying fluid flow (Thomas *et al*., 2013). KHI manifest in two-fluid systems (such as water-air) that are stratified by density variations with a velocity differential between the fluids (Miles, 1959). Shear forces generated from the velocity difference lead to unstable vortices at the interface which grow exponentially until the distorted interface overturns into spiral forming rippled features (Funada and Joseph, 2001).

Streptococcus mutans is a gram-positive and facultative anaerobic microorganism that is considered a causative agent of human dental decay (Loesche, 1986). *S. mutans* biofilms have been widely used in research to investigate biofilm mechanical properties and detachment (Vinogradov *et al*., 2004; Cense *et al*., 2006). We previously performed high-speed camera (HSC) videography during the exposure of *in vitro S. mutans* interproximal dental biofilms to high-velocity (60 m/s) impacts from micro water jets and sprays using an interdental cleaning device [AirFloss (AF), Philips] (Rmaile *et al*., 2013; 2014; 2015; Fabbri *et al*., 2015). We demonstrated that biofilms exhibited fluid-like behaviour on the order of milliseconds in response (Fabbri *et al*., 2015). The videos not only recorded a quasi-instant biofilm fluidisation, but also suggested the formation of migratory ripple-like structures.

Since microsprays generated from the AF device have very complex flow hydrodynamics and proceed through a series of pulses (Rmaile *et al*., 2014), here, we used a well-defined and steady compressed air jet that allowed the study of the rippling phenomenon under conditions where flow rate could be controlled. We report for the first time that ripple-like structures (i.e., series of small surface waves that propagate along the interface between differing media) in *Streptococcus mutans* and *Staphylococcus epidermidis* biofilms and wrinkle-like structures (i.e., deformations caused by compression when a material is 'bunched' together) in *Pseudomonas aeruginosa* biofilms can form extremely rapidly. We modelled the observed ripple morphology using a multiphase model (Cogan and Keener, 2004). Theoretical treatment of the process as a Kelvin–Helmholtz instability indicated that the rippling phenomenon was primarily due to physics rather than chemistry or biology. In addition, we discovered that biofilm viscosity can dramatically influence instability formation explaining the different surface corrugations observed. Turbulence through Kelvin–Helmholtz instabilities occurring at the interface demonstrated that the biofilm flows like a viscous liquid under high flow velocities applied within milliseconds. KHI are a prelude to mixing and turbulence (Geyer *et al*., 2010) and direct evidence of their formation in biofilms has potentially important implications for disruption of gradients and microniches, antibiotic delivery and mechanical removal and dissemination.

Results and discussion

Ripples formation in S. mutans *biofilms exposed to rapid high velocity microsprays*

Recently, we had developed a microfluidic flow channel system for investigating rapid high velocity water and air microspray interactions with *S. mutans* biofilms for dental cleaning applications (Fabbri *et al*., 2015). HSC videography suggested the formation of migratory ripple-like structures at the biofilm/fluid interface. Considering the intriguing nature of this phenomenon, in the present study we used an identical setup in order to allow these structures to more fully develop.

S. mutans biofilms were grown on glass microscope slides for 72 h in a BHI + 2% sucrose + 1% mucin medium. The microfluidic flow channel was created by inserting two biofilm-colonized glass microscope slides in parallel separated by a distance of 1 mm into a specially fabricated holder. *S. mutans* biofilms were exposed to either a water or an air microspray burst. HSC movies of

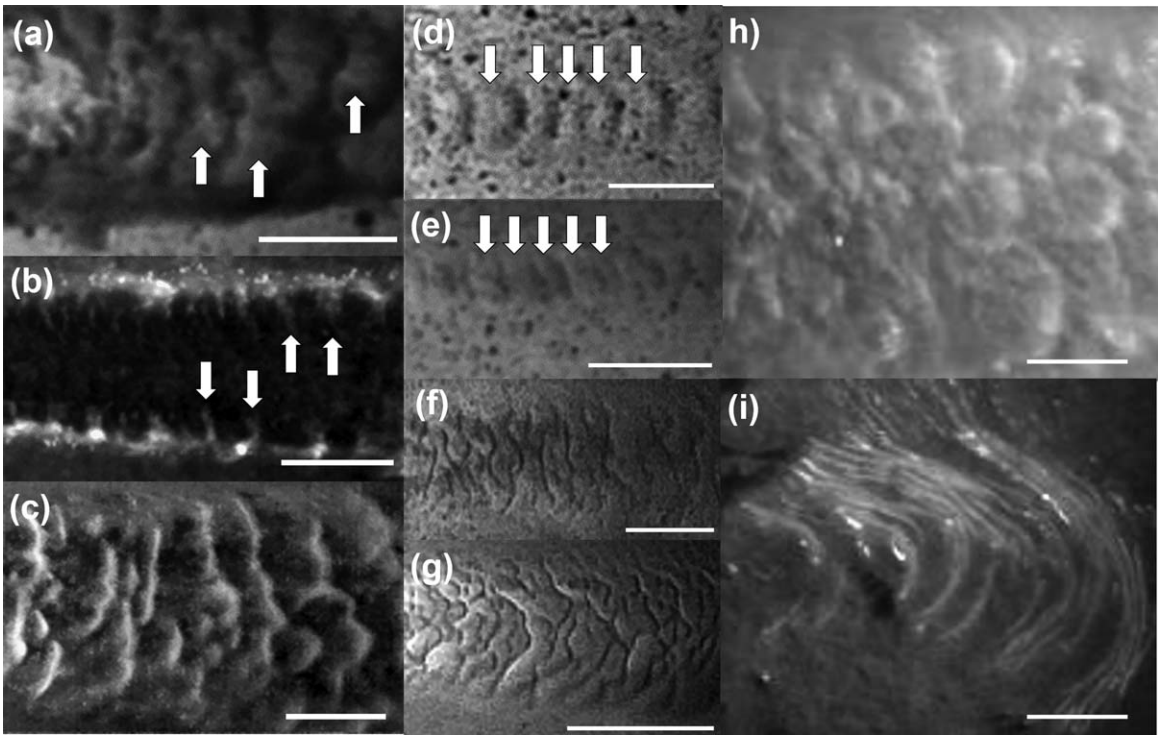

Fig. 1. High magnification pictures from HSC videos of different ripples and wrinkles morphologies during biofilms exposure to rapid high-velocity fluid flows.
A–C. *S. mutans* biofilms exposed to high-velocity air and water microsprays (A) The water microspray burst generated thick crescent-shaped ripples at the front edge of the burst.
B. The air microspray generated arcuate ripples (white arrows) at the edges of the clearance zone.
C. Crescent-shaped ripples at the front edge of the air microspray. Flow was left to right. Scale bar = 2 mm.
D–G. Three-day old *S. mutans* biofilms exposed to a compressed air jet of 24.6 m/s (D), 44.9 m/s (E), 68.1 m/s (F), 85.5 m/s (G).The ripples pattern changed as air jet velocity increased. Panel (D) and (E) show thin, parallel ripples appeared during low-velocity air jets (24.6 m/s and 44.9 m/s).
F. Transition from parallel to crescent-shaped at 85.5 m/s.
G. Complex crescent-shaped at high velocities (110.1 m/s). Scale bar = 5 mm.
H, I. Ripples formed in S. *epidermidis* biofilm (H) and wrinkles formed in *P. aeruginosa* biofilm (I) during the exposure to an air jet of 85.5 m/s. Flow was left to right. Scale bars are 2 mm.

S. mutans biofilms exposed to a high-velocity water microspray (Supporting Information Video S1) or an air microspray (Supporting Information Video S2) showed the burst rapidly entered the microchannel forcing the biofilm downstream and out of the device as it created a clearance zone through the body of the biofilm. Migratory ripple-like structures developed within ms at the fluid-biofilm interface. The ripple structures travelled with an average velocity of 1.87 ± 0.27 m/s and 2.69 ± 0.07 m/s during the water microspray and air bursts respectively. Immediately, after the burst, the ripples began to dissipate leaving little trace of their formation (Supporting Information Video S3). Different ripple patterns were observed at different phases of the bursts. The water microspray generated thick crescent-shaped ripples (Fig. 1A) with an average wavelength of 1.85 ± 0.02 mm and width of 0.31 ± 0.03 mm. The air microspray first produced curved ripples protruding from the biofilm into the channel created by the air with an average amplitude of 0.57 ± 0.11 mm (Fig. 1B). Then, thicker crescent shaped-ripples developed at the leading edge of the air burst with an average wavelength of 1.12 ± 0.04 mm and a width of 0.2 ± 0.04 mm (Fig. 1C). We noticed similarities in the ripple morphology of these high-velocity ripples to the slow moving, long-lived ripples observed in previous studies (Stoodley *et al.*, 1999b; Purevdorj *et al.*, 2002) for biofilms grown under steady liquid flows of 1 m/s ($Re = 3000$). However, our videos demonstrate that ripples can also form and migrate at extremely fast time scales (ms) when exposed to high velocity fluid flow.

Ripples formation in S. mutans *biofilms exposed to air jets at different velocities*

Microsprays generated from the AF device have very complex flow hydrodynamics (Rmaile *et al.*, 2014), therefore,

Table 1. Average air jet velocities (u_{jet}) entering the microchannel with the associated *Re* and τ_w developing on S. mutans biofilms.

U_{jet} (m/s)	*Re*	τ_w (Pa)
7.2	780	0.6
24.6	2667	4.1
44.9	4867	11.5
68.1	7382	23.8
85.5	9268	35.5
110.1	11 935	55.3

All SDs were below 34% of the means.

ripples morphology variation was also caused because of the velocity changes in the flow itself. To study the phenomenon under conditions where flow rate could be controlled we used a well-defined compressed air jet of seven different velocities (Table 1). The Reynolds number (*Re*) and the relative wall shear stress (τ_w) in the biofilm-exposed zones were calculated according to Stoodley *et al*. (1999a) (Table 1). The transition between laminar and turbulent flow in rectangular channels occurs at *Re*$\sim$2500 (Hanks and Ruo, 1966), therefore, the lowest velocity of 7.2 m/s ($Re = 780$) will be laminar, but higher velocity air jets would be in the turbulent regime. Turbulent flow is mainly found in fast moving streams and rivers ($Re = 10^5 - 10^6$), industrial pipelines, ship hulls ($Re =$ up to 10^9) and water irrigators for oral health and surgical debridement. Using the same microfluidic flow channel system as previously, *S. mutans* biofilms samples were exposed to the air jets. HSC movies of *S. mutans* biofilms showed there was no ripple formation at the lowest air flow of 7.2 m/s ($Re = 780$) but they did occur at flows greater than 24.6 m/s ($Re = 2667$) (Supporting Information videos S4–8). Ripples generated at 24.6 m/s (Fig. 1D) and 44.9 m/s (Fig. 1E) were thin, straight and parallel to the flow direction whereas ripples formed at 68.1 m/s (Fig. 1F) and 85.5 m/s (Fig. 1G) had more complex crescent-patterns. The ripple velocity increased exponentially ($R^2 = 0.972$), with increasing air jet velocity, from $u_R = 0.22 \pm 0.02$ m/s at $u_{jet} = 24.6$ m/s to $u_R = 2.27 \pm 0.16$ m/s at $u_{jet} = 110.1$ m/s (Fig. 2A, black dots), while wavelength decreased exponentially ($R^2 = 0.972$), from $w_R = 1.85 \pm 0.16$ mm at $u_{jet} = 24.6$ m/s to $w_R = 0.68 \pm 0.07$ mm at $u_{jet} = 110.1$ m/s (Fig. 2B, black dots). Anova followed by Tukey–Kramer tests showed statistical difference within the two set of data (velocity and the wavelength) between low velocities and high velocities. The morphology of the generated ripples was similar to the ones discovered in annular thin ($\sim$ 147 μm) liquid films exposed to high gas velocities ($>$ 20 m/s) (Asali and Hanratty, 1993) and their formation has been explained by interfacial instability as the fluids flow past each other (Cohen and Hanratty, 1965; Craik, 1966). Although our wavelength values were lower by a factor of $\sim 10^{-1}$ than the ones measured by Asali *et al*. (Asali and Hanratty, 1993), the same trend was observed.

Fast Fourier Transform (FFT) was also used to determine whether there were dominant frequencies in the ripple pattern. Below an air jet velocity of 68.1 m/s, the spectrum was relatively simple, whereas at the higher velocities of 85.5 m/s and 110.1 m/s there was more fluctuation. Some of this noise could be due to the imaging itself. However, studies showed that a transition to turbulence is bordered by an instability which can increase the randomness of the FFT spectra (Joseph and Renardy, 2013). In addition, similar FFT spectra were found in a computational model on rippling in biofilms colonies subject to external forcing (L. Jian *et al*., in preparation). Despite this noise distinct peaks are identifiable in the data: the major peaks identified in the FFT spectrum for each air-jet velocity corresponded to wavelengths values were similar to the ones measured using Fiji (Supporting Information Fig. S1).

Ripples and wrinkles formation in S. epidermidis *and* P. aeruginosa *biofilms*

We hypothesised that the formation of rippling patterns might likewise be a general phenomenon to bacterial biofilms given the right set of biological and environmental conditions. We tested our hypothesis by exposing biofilms grown from *S. epidermidis* (a skin isolate and opportunistic biofilm pathogen in orthopaedic device related infections) or *P. aeruginosa* (a common nosocomial biofilm pathogen infecting wounds, medical devices and the upper respiratory tract) to a steady air jet of velocity $u_{jet} = 85.5$ m/s ($Re = 9268$). *S. epidermidis* biofilms formed ripples which were morphologically similar to the *S. mutans* ripples at the equivalent air jet velocity (Supporting Information Video S9, Fig. 1H) which were crescent-shaped with wavelengths of 1.2 mm $\pm$ 0.08 mm and widths of 0.23 mm $\pm$ 0.04 mm moving at a velocity of 1.7 m/s ($\pm$0.5, $n = 5$) (Fig. 2A). In contrast, the *P. aeruginosa* biofilms were pushed forwards but the air jet did not create a channel through the biofilm. Wrinkle-like structures formed rather than ripples as the biofilm bunched up against the downstream portion which remained attached and was not moved (Supporting Information Video S10 and Fig. 1I). The widths of the wrinkles were 0.18 mm $\pm$ 0.03 mm. Unlike the ripples, the wrinkles did not migrate over the surface after they had formed but resisted the air jet for approximately 300 ms. During this time the wavelength of the wrinkles decreased from 1.1 mm $\pm$ 0.3 mm to almost 0 mm as the biofilm was increasingly compressed against the biofilm downstream (Fig. 2B). After 300 ms the whole biofilm detached from the surface and was pushed out of the flow cell as a plug.

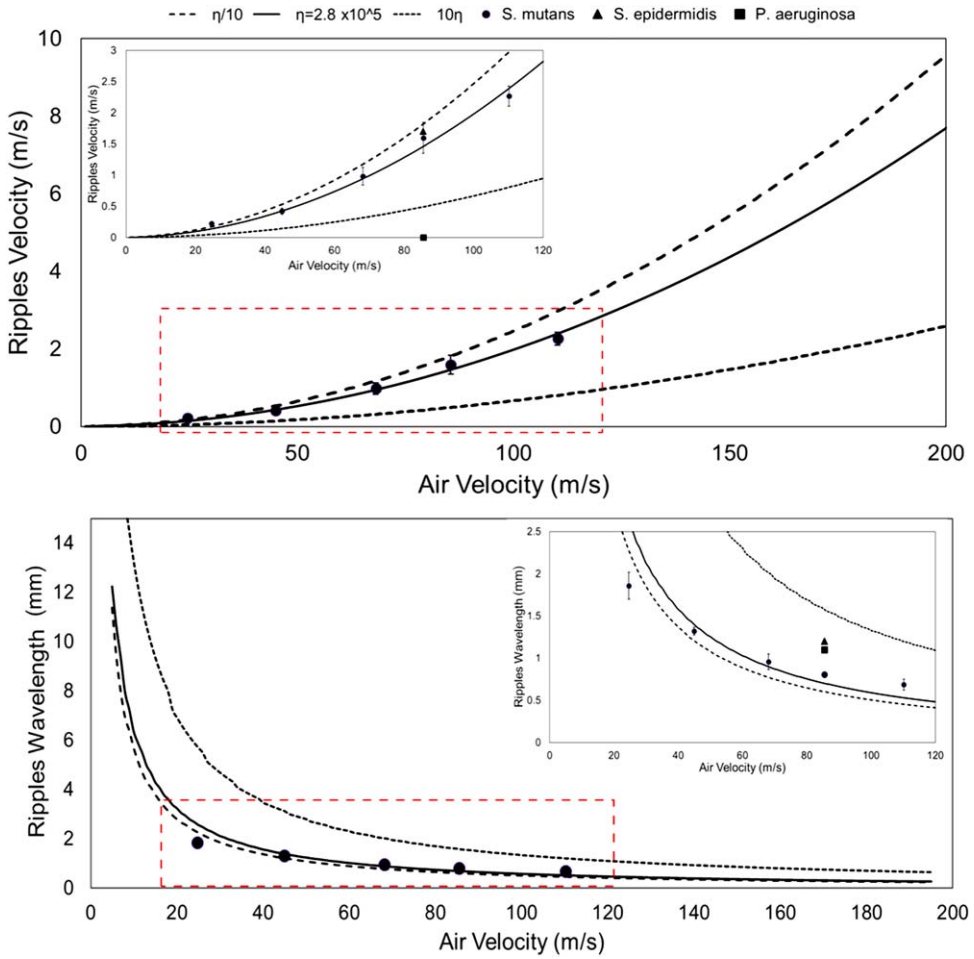

Fig. 2. Comparison between the theoretical predictions (lines) and the experimental measurements (symbols) of ripples' velocity and wavelength as a function of the air jet velocity for *S. mutans*, *S. epidermidis* and *P. aeruginosa* biofilms. Solid line represents the predicted data using a base viscosity ($\eta_B = 2.8 \times 10^5$ Pa·s) whereas dashed lines a low viscosity value (η/10) and a high viscosity value (10 η) to cover a range of three orders of magnitude. Experimental data of *S. mutans* (•), *S. epidermidis* (▲) and *P. aeruginosa* (■) biofilms are represented as means ± 1 SD from three independent replicates.
A. The measured ripples' velocity for *S. mutans* biofilms increased exponentially ($R^2 = 0.957$ for exponential fit) with the air jet velocity. Predicted values using the base viscosity value agreed well with the experimental data ($R^2 = 0.99$) for *S. mutans* biofilm. Ripple velocity for *S. epidermidis* at $u_{jet} = 85.5$ m/s was inside the range of predicted data. The inset plots represent data from $u_R = 0$–3 m/s.
B. The measured ripples wavelength for *S. mutans* biofilms decreased exponentially ($R^2 = 0.989$ for exponential fit) with the air jet velocity. Predicted values using the base viscosity value agreed well with the experimental data ($R^2 = 0.98$) for *S. mutans* biofilm. Ripple wavelengths for *S. epidermidis* and *P. aeruginosa* were inside the range of predicted data. The inset plots represent data from $\lambda_R = 0$–2.5 m/s. [Colour figure can be viewed at wileyonlinelibrary.com]

Biofilm ripples as Kelvin–Helmotz instabilities

The formation of ripples at the interface of the biofilm and the high velocity air jet occurred within milliseconds, suggesting that the phenomenon was not likely to be a sedimentary-like process of erosion and deposition but more likely a shear flow induced interfacial instability (Tauber *et al*., 2002). KHI occur when immiscible, incompressible and inviscid fluids are in relative and irrotational motion (Matsuoka, 2014). To test our hypotheses, we performed a classical KHI linear stability analysis to estimate the correlation between the ripple wavelength and air velocity (See Supporting Information Materials and Methods). Classical analysis assumes the fluids are simple Newtonian materials. We considered a two-fluid system formed by a top fluid (air), moving initially horizontally with velocity u_a and a bottom fluid (biofilm), initially stationary (Supporting Information Fig. S2). To reflect the biofilm structure, we modelled the second fluid using a widely accepted model for the biofilm material referred to as a multiphase model that assumes that the biofilm is composed of both fluid and solid components (e.g., encapsulated water and EPS/bacterial components) (Cogan and Keener, 2004; Klapper and Dockery, 2006; Winstanley *et al*., 2010; Seminara *et al*., 2012). In practice, this allows the theory to focus on a variety of physical,

chemical and biological processes since the model separates the constituent parts of the biofilm. Therefore, rather than using a lumped constitutive relationship, the model allows for a distinction between forces that affect the EPS and those that affect the fluid. Additionally, the multiphase framework allows for natural implementation of non-Newtonian properties via the interaction between the solid and liquid components of the biofilm. We used a baseline biofilm viscosity (η) of 2.8×10^5 Pa.s, which was the mean η measured on similar *S. mutans* biofilms (Vinogradov *et al.*, 2004). From the linear stability analysis (see Supporting Information) we obtained a dispersion curve, that relates the perturbation wavelength, k, and the growth rate, ω, of the perturbation:

$$-\omega^2 + M\omega + N = 0, \tag{1}$$

where the coefficients are

$$M = 2ku_1 - i\ B\ k - 2\ i\ k^2(\mu_f + 2\mu_s), \tag{2}$$

$$N = -k^2 u_1^2 + \gamma k^3. \tag{3}$$

The viscosities are explicit in Eqs. (1–4). The dispersion curve has a unique maximum (peak) that depends on the air jet velocity in a complicated nonlinear way (Supporting Information Fig. S3). The peak indicates the most unstable mode and is used to estimate the ripples wavelength and velocity. From a pattern formation standpoint, we expect that the observed wavelength will correspond to this maximum since it is growing the fastest. The peak gives a good estimate for the observable wavelength until nonlinear effects such as mixing take over

The model predicted an exponential dependence of the ripple velocity and wavelength on the air jet velocity (Fig. 2). An excellent agreement (*R*-squared$\sim$99%) was observed between the experimental measurements of the ripples velocity for *S. mutans* biofilms and the data obtained from the analysis using η_B (Fig. 2A). Whereas, the experimental measurements of the ripples wavelength for *S. mutans* biofilms were in good agreement (*R*-squared $>$ 98%) with the model using a viscosity in the range $1/10\eta_B$ - η_B (Fig. 2B). The key process involved in the ripple formation is, therefore, a KHI implying viscous fluid behaviour of *S. mutans* biofilms during rapid high shear stresses. This implies that the rippling phenomenon is likely dominated by physical interactions. The details of the material properties, surface tension, air jet velocities, and so forth serve to scale the predicted pattern. We noted that we need some level of detail regarding the material properties of the biofilm (such as shear thinning or elasticity) to match the observed air jet velocity/wavelength relationship since a simple Stokes fluid approximation of the biofilm had a much poorer match (data not shown). It appears that viscoelasticity does not play a substantial role except possibly at lower velocities, based on the agreement between the model and the data. The wavelength in the theory increases faster than the measurements for low velocities, therefore, is more likely that for low forcing velocities elastic properties might need to be included. However, in the future, modelling viscoelastic behaviour can be included to see any changes in the ripples characteristic.

Whether a biofilm is more likely to flow in ripples or form more solid-like wrinkles is likely a function of a number of factors such as biofilm viscosity. Therefore, we assessed the influence of biofilm viscosity on KHI formation performing the same analysis using biofilm viscosity values of 1/10x and 10x the baseline value. Changing the viscosity has the effect of changing the peak of the dispersion curve. Although the relationship is quite complicated, generically the wavelength/velocity curve moves up and right with increasing viscosity (Fig. 2) implying that the wavelengths are typically higher for the same bulk velocity as viscosity increases. *S. epidermidis* ripple wavelength and velocity values fell within the predicted range for the chosen viscosities, whereas *P. aeruginosa* wrinkles did not migrate over the surface ($u = 0$, Fig. 2). This implies that *P. aeruginosa* biofilm has a higher viscosity than the ones we had assumed.

Finally, our data supports the hypothesis by Thomas *et al*. regarding a possible mechanism for ripples formation in Kinneyia fossils (Thomas *et al*., 2013). Kinneyia are a type of microbially mediated sedimentary structures (MISS) (Noffke *et al*., 2001; 2013) characterised by an undulating ripple-like pattern with a wavelength on the millimetre to centimetre scale. The researchers proposed that the key mechanism involved in the ripples formation is a KH instability induced in a viscoelastic film subjected to flow in the overlying fluid. However, these interfacial instabilities were demonstrated in gels, not living biofilms. In addition, in contrast to our findings, they showed that the ripples wavelength was independent on the viscosity and the flow velocity. Additionally, it should be noted that we assume direct coupling between the surface flow and the biofilm flow via an interface condition (continuity) while they impose a pressure condition. Thus, although their dispersion curve predicts a relation to the height, the form of their pressure dependence obscures other nonlinearities.

Biofilm fluid behaviour

Literature on biofilm mechanics showed a progression of behaviours as shear loading is increased from an elastic solid (no hysteresis), viscoelastic solid (hysteresis but no permanent deformation), viscoelastic liquid (both elastic recoil and viscous flow) and finally viscous liquid (Klapper

et al., 2002; Stoodley *et al.*, 2002b). Here, we documented that when exposed to high shear stresses *S. mutans* biofilm behaved immediately as a liquid and it was only after the flow was removed that the viscoelastic recoil of the biofilm was observed (Supporting Information Video S3). A similar behaviour was seen in *S. epidermidis* biofilm. However, in *P. aeruginosa* biofilms the wrinkles structures we observed were similar to those described by Trejo *et al.* in *Bacillus subtilis* biofilm pellicles (2013) suggesting cohesive attachment failure at the biofilm-substratum interface resulting in wrinkling rather than true flow. The authors also showed that eps mutant biofilms had no elastic response highlightening the key role of the matrix in providing the elasticity of the pellicle for forming the wrinkling process. We speculate that the differences in the response of *P. aeruginosa* biofilm to that of *S. mutans* or *S. epidermidis* biofilms was due to differences in the EPS chemistry and mechanical properties.

Microscopic structure of ripples and wrinkles

Changes in the EPS composition can considerably change biofilm mechanical behaviour which can affect biofilm detachment and proliferation (Flemming, 2016). Therefore, we went on studying how cell packing and spatial EPS organization through the biofilm change as ripples form using confocal laser scanning microscopy (CLSM) and scanning electron microscopy (SEM). Plan views of confocal images of *S. mutans* biofilms prior to exposure to water microsprays showed a relatively uniform biofilm covering the surface (Fig. 3A). The cross section showed that cells were evenly distributed and the film was approximately 20 μm thick (Fig. 3B). After exposure to the microspray the remaining biofilm in the area where the ripples had formed adjacent to the clearing zone showed a heterogeneous pattern of cell clusters separated by areas where biofilm was completely removed (Fig. 3C). Cross-sections through the clusters in these areas showed that the cells were more densely packed and the clusters were approximately 5 μm thick (Fig. 3D). The cell-density measured in the ripple area ($1.4 \times 10^6 \pm 2.8 \times 10^5$ cells/mm^2) was significantly higher than the cell-density measured in the undisturbed areas ($5.7 \times 10^5 \pm 1.6 \times 10^3$ cells/mm^2; $p = 0.01$) (Fig. 3E). The fact that the cell density was increased by a factor of 3 but the thickness was reduced by a factor of 4 after the ripple formation suggests that much of the loss in thickness could be attributed to compression rather than detachment of the top layer of biofilm. We hypothesize that the water microspray might have altered the biofilm structure by 'squeezing' water out or by rearranging the EPS matrix structure. Mechanical compression and tensile tests on biofilms formed by *S. mutans*, *P. aeruginosa* and *S. aureus* and mixed species biofilms show that the biofilms become stiffer as they are compressed or pulled (Rupp *et al.*, 2005; Fabbri and Stoodley, 2016) demonstrating a J-shaped stress-strain curve (Klapper *et al.*, 2002). Such a curve can be explained by dewatering, even if the biofilms are fully submerged. As mechanical stresses are applied to the biofilm the squeezing of water out of the matrix would cause the EPS polymer strands to become denser and forced closer together thus becoming increasingly stiffer. Future work will focus on looking at EPS ultrastructure using techniques such as transmission electron microscopy (TEM) or stimulated emission depletion (STED) microscopy. Also, staining the EPS with appropriate lectins and then analysing with CLSM could give further information about spatial EPS organization. SEM images of the *S. mutans* biofilms not exposed to high velocity fluid flow, showed a structure with an undulating surface interspersed with prominent clusters of cocci (Fig. 4A) arranged in towers (Fig. 4B). The *S. epidermidis* biofilm were more compact than the *S. mutans* biofilms with a dense layer of cocci and less pronounced clusters (Fig. 4C and D). The *P. aeruginosa* biofilms showed rod-shaped cells embedded in an undulating EPS matrix (Fig. 3F). Higher magnification revealed that some clusters had cells which were interconnected by fibre-like structures (white arrows, Fig. 4F). Although macroscopically the ripples rapidly dissipated after the fluid flow was removed, SEM showed residual structures. In the *S. mutans* biofilms the cells had been rearranged in dense parallel ridges (Fig. 5A and B). The *S. epidermidis* biofilms showed similar band structures but these were much fainter and appeared to be on the glass surface. Individual cocci were arranged on the bands (Fig. 5C and D). In the *P. aeruginosa* biofilms there were a base layer of single cells and intriguing parallel bands. The bands, perpendicular to the flow, were possibly dehydrated EPS, suggesting that the EPS had been concentrated into ridges during the wrinkling. It is known that the dehydration process significantly alters biofilms three-dimensional structure due to EPS polymers collapsing (Fassel and Edmiston, 1999). Therefore, these bands were likely more voluminous than seen in the SEM.

Conclusions

HSC videography on laboratory-grown single-species biofilms exposed to rapid high-velocity fluid (water and/or air) flows allowed the discovery of transient surficial corrugations, which migrated over the biofilm surface. In particular, we documented flowing ripples formed in *S. mutans* and *S. epidermidis* biofilms and wrinkles in *P. aeruginosa* biofilms when exposed to a well-defined compressed air jet. We found that the measured ripples' wavelength and

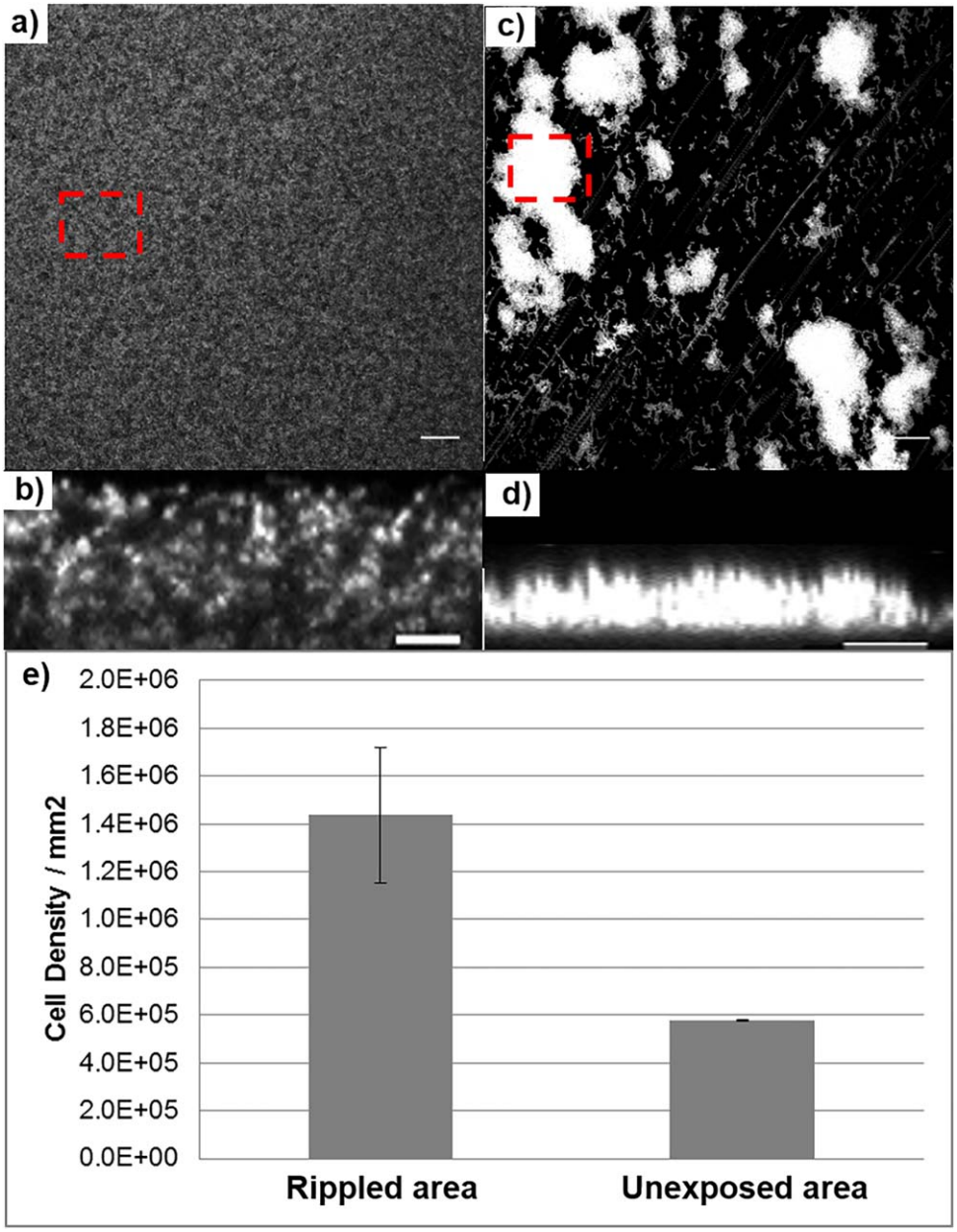

Fig. 3. Cell density distribution in *S. mutans* biofilms before and after the microspray exposure. Confocal images in *x–y* plane view (maximum projections) of *S. mutans* biofilm without any treatment (control) (A) and after the water microspray exposure (B). Scale bars are 20 μm. *x–z* Cross sections taken at selected position in the *x-y* plan view (red boxes) without any treatment (control) (C) and after the water microspray exposure (D, E). Scale bars are 5 μm. (E). Bar chart showing cell density over mm^2 in *S. mutans* biofilms measured in the rippled area (as shown in (A) and (B)) compared with the cell-density measured in the controls. Data represented as mean ± 1 SD, $n = 3$. Values are statistically different ($p < 0.05$). [Colour figure can be viewed at wileyonlinelibrary.com]

velocity were dependent on the air jet velocity. Using a detailed physics-based model and classical mathematical analysis, we showed that the rippling process is primarily due to physics providing support for the evidence that ripples are KHI and suggesting the onset of turbulence in the biofilm. In addition, the analysis demonstrated that biofilm viscosity modulates KHI formation and, therefore, the type of corrugation.

The agreement among the modelling and the experimental measurements implies viscous fluid behaviour of *S. mutans* biofilms during rapid high shear stresses. The ability of biofilm to flow and migrate in ripples when exposed to transient high-velocity fluid flows has important consequences for mechanical removal strategies in the medical field or spread of pathogens. Fluid/structure interactions in biofilms are known to modulate the dynamics of biofilm growth, tolerance to antibiotics and virulence. This phenomenon might also explain our recent finding that high-velocity water sprays more effectively delivered microbeads and antimicrobials into in vitro dental biofilms (Fabbri *et al.*, 2016). Interfacial instabilities in biofilms may enhance mass and heat transport (Chen *et al.*, 1997; Vazquez-Una *et al.*, 2000). Finally, our discovery of different observable patterns in biofilms offer the opportunity for theoretical models to be tested against specific and repeatable observations. These models are used, in turn, to

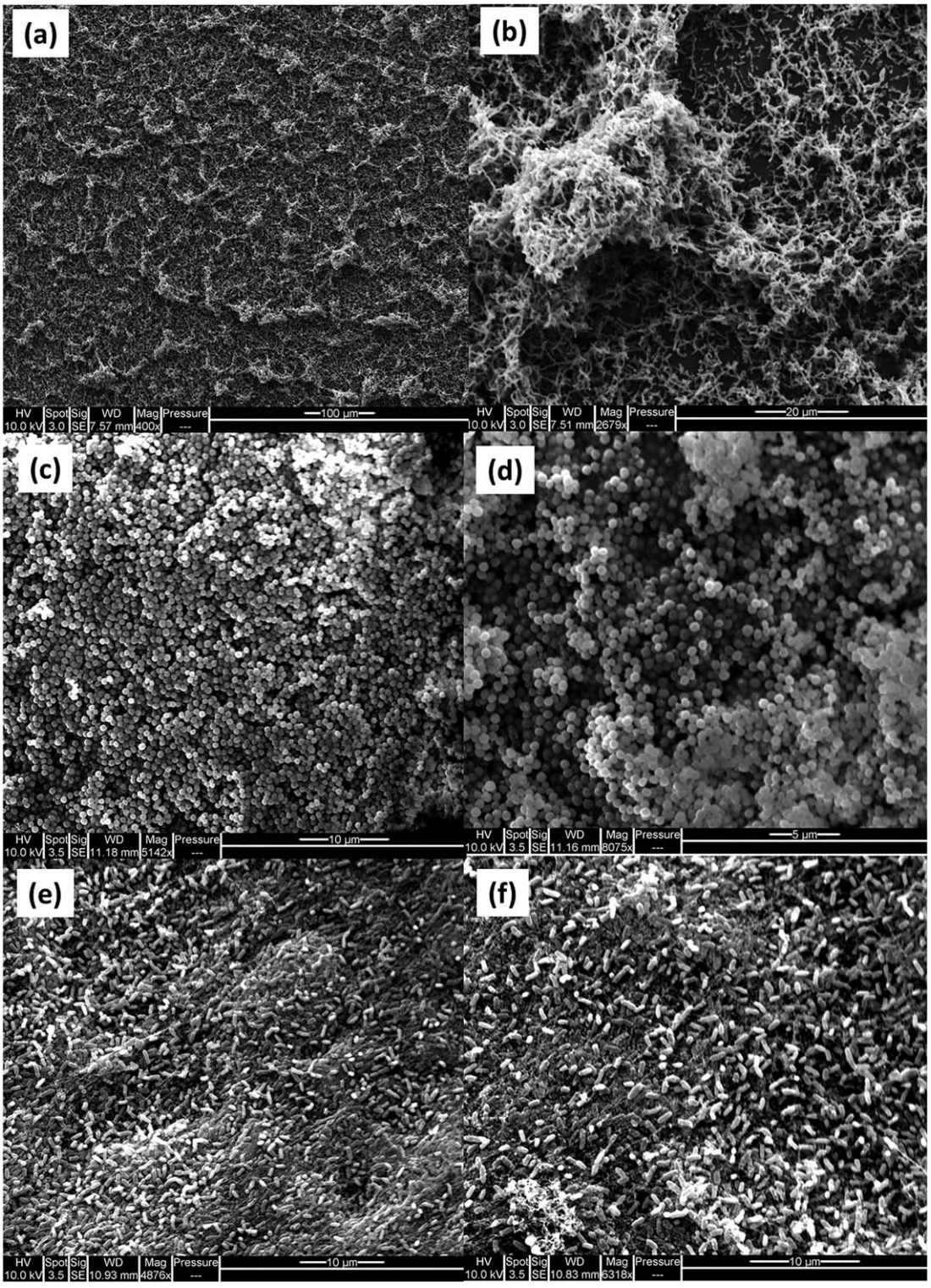

Fig. 4. Scanning electron microscope images showing *S. mutans* biofilm (A, B), *S. epidermidis* (C, D) and *P. aeruginosa* (E, F) prior to exposure to high velocity fluid disruption.

A. A background layer interspersed with larger *S. mutans* cell clusters is presented.

B. Higher magnification SEM image of *S. mutans* biofilm clusters shows they were composed of dense clusters and chains of cocci.

C. D. *S. epidermidis* biofilm presents a background layer formed of sphere-shaped cells.

E, F. *P. aeruginosa* biofilm presents rod-shaped cells interconnected by fibre-like structures, which is likely dehydrated EPS.

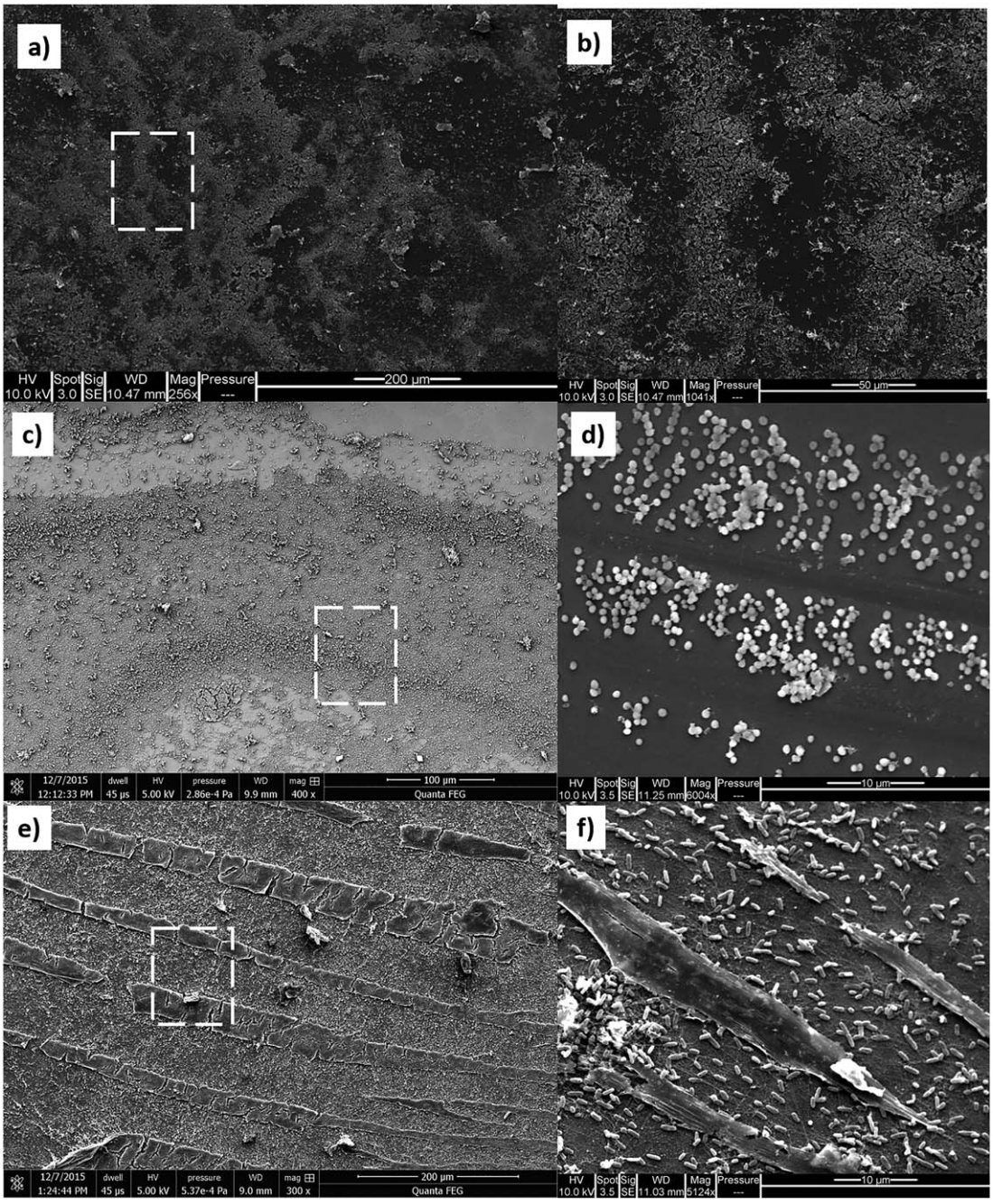

Fig. 5. Low and high-magnification of scanning electron microscope images showing various ripple-like patterns formed in *S. mutans* (A, B), *S. epidermidis* (C, D) and *P. aeruginosa* (E, F) biofilms after the exposure to high velocity fluid disruption.
A, B. The *S. mutans* biofilms shows cells rearranged in dense parallel ridges.
C, D. The *S. epidermidis* biofilms showed similar ridges on which individual cocci were arranged.
E, F. In the *P. aeruginosa* biofilms there were a base layer of single cells and parallel bands of material which was likely EPS, perpendicular to the flow.

quantify important features of biofilms [such as the role of surface tension (Picioreanu *et al.*, 2001)], explore aspects of biofilms not available for experimental studies (Cogan, 2010; Friedman, 2015), and to optimize removal protocols (De Leenheer and Cogan, 2009).

Experimental procedures

Bacteria and growth media

Overnight cultures of *S. mutans UA159* (ATCC 700610), *S. epidermidis* (ATCC 35984) and *P. aeruginosa* PAO1

were grown in 2% sucrose-supplemented brain-heart infusion (BHI + S, Sigma-Aldrich), tryptic soy broth (TSB, Oxoid) and M9 medium respectively. The M9 medium consisted of 500 ml of M9 salts solution (Formedium), 1 ml of 1M $MgSO_4$ (Sigma-Aldrich), 50 μl of 1M $CaCl_2$ (Sigma-Aldrich) and 10 ml of 20% Glucose (Sigma-Aldrich). Each overnight culture was diluted in fresh media to an optical density value corresponding to 10^6 cfu/ml for inoculation.

Biofilm growth

S. mutans biofilms were grown on autoclaved glass microscope slides (75 mm × 25 mm, Corning, Sigma-Aldrich). The slides were placed in petri dishes and conditioned with 10 ml of BHI + S and 1% type II porcine gastric mucin (Sigma-Aldrich; BHI + SM) to simulate salivary proteins and establish a conditioning film. Then the conditioned-slides were inoculated with the *S. mutans* adjusted-overnight culture and grown under static conditions for 72 h at 37°C and 5% CO^2 with medium replacement every 24 h. *S. epidermidis* and *P. aeruginosa* biofilms were grown similarly on glass slides (but with no mucin conditioning) for 72 h or 7 days respectively at 37°C in a humidified incubator with replacement of their media every 24 h.

Microchannel flow system

Previously we had developed a microfluidic flow channel system (Fabbri *et al*., 2015) to study the removal of dental biofilms by high velocity jets and sprays. Briefly, the flow channel was created by inserting two biofilm-colonized glass microscope slides in parallel separated by a distance of 1 mm into a specially fabricated holder. The glass slide enabled high-speed imaging [recorded at between 500 and 8000 frames per seconds (fps)] with a HSC MotionPro X3 (IDT) equipped with a Sigma 105 mm f/2.8 EX DG Macro lens. Illumination was provided by two optical fibre light sources (MH-100, Dolan Jenner Industries Inc.). After the growth period, biofilm covered-slides were gently rinsed in 1% phosphate-buffered saline (PBS) solution (Sigma-Aldrich) to remove loosely adhered cells before being placed in the microchannel system.

Biofilm exposure to high-velocity microsprays

First, *S. mutans* biofilms were exposed to either a water or an air microspray burst delivered from a commercially available oral hygiene device (Philips AirFloss) as previously described (Fabbri *et al*., 2015). The device was filled either with water to generate a water microspray, as per normal use of the device, or was left empty in order to generate an air microspray. The water microspray lasted 60 ms and dispensed 130 ± 0.03 μl ($n = 11$) of water dispersed as a discrete burst of micro drops in air. The device was convenient since it could generate high velocity fluid flow and the generation of liquid waste was minimized (Fabbri *et al*., 2015).

Biofilm exposure to air-jets

An air piston compressor was used to generate a velocity-controlled air-jet (ClassicAir 255, Metabo). The average air jet velocities (u_{jet}) entering the microchannel (Table 1) were determined from the volumetric air flow rate (Q_{jet}), measured using a rotameter (FR2000, Key Instruments), from:

$$u_{jet} = \frac{Q_{jet}}{A^*} \tag{4}$$

$$D_h = \frac{A^*}{P} \tag{5}$$

where D_h is the hydraulic diameter, A^* and P are the area (1.92×10^{-3} m^2) and the perimeter (5.57×10^{-3} m) of the nozzle (Supporting Information Fig. S4).

The air jet, as it passed through *S. mutans* biofilms, generated a clearance area where the biofilm was removed. The Reynolds number (*Re*) and the relative wall shear stress (τ_w) in the clearance area were calculated according to Stoodley *et al*. (1999a) (Table 1). In this case D_h was derived from the depth of the microchannel (distance between the slides, $D = 1$ mm) and the width (W) of the clearance area, measured 10 mm far from the inlet ($W = 4.5 \pm 0.4$ mm). *Re* has been calculated according to the following equation:

$$Re = \frac{u_{jet} \cdot \rho \cdot D_h}{\eta} \tag{6}$$

where ρ and η are the density and viscosity of air at 20°C and 1 atm. Assuming fully developed laminar flow through the microchannel, the associated wall shear stress (τ_w) was measured using:

$$\tau_w = \frac{8 \cdot \nu \cdot u_{jet}}{D_h} \tag{7}$$

Instead for turbulent flow, the following equation was used:

$$\tau_w = \frac{f \cdot {u_{jet}}^2 \cdot \rho}{2} \tag{8}$$

where f is the fanning friction factor ($f = \frac{0.0791}{Re^{0.25}}$, for turbulent flow).

S. epidermidis and *P. aeruginosa* biofilms were exposed to $u_{jet} = 85.5$ m/s ($Re = 9268$).

High-speed camera image-processing

Videos were analysed with the image-processing package Fiji (Schindelin *et al*., 2012). The videos were converted to tiff stacks with each frame in the stack being a different time (T) so that the stack could be represented in XYT co-ordinates. Ripples wavelength (λ_R) and width (w_R) were measured using the plot profile function (Supporting Information Fig. S5A and B). The ripples' velocity (u_R) was measured using the reslice function which creates a time-trace along a line drawn across the ripple (Supporting Information Fig. S5C). Fast Fourier Transform (FFT) was used to determine whether there were dominant and secondary frequencies in the ripple pattern

formed during the *S. mutans* biofilm exposure to air jets. First profile plots were obtained from individual frames. This produced a graph showing peaks (dark pixels) and valleys (light pixels) corresponding to ripples and the spaces between them. Next, FFT analysis was performed on the plot profile data. The major peaks corresponding to dominant frequencies were identified by eye. Wavelengths were obtained from the inverse of the relative peak frequencies.

Confocal microscopy

S. mutans biofilms were fixed with 4% Paraformaldehyde (PFA) solution to preserve structure (von Ohle *et al.*, 2010) and the cells were stained with the nucleic acid stain Syto 63 (Invitrogen). Following a rinse in 1% PBS solution for 5 secs, the slides were gently covered with a cover slip and inverted. Confocal laser scanning microscopy (CLSM) was performed using an inverted Leica DMI600 SP5 (Leica Microsystems). In order to assess the influence of the high velocity flow on internal restructuring, we measured cell-density from confocal stacks of biofilm exposed to the water microspray using the Fiji software. First, we selected a region of interest (ROI) where there was remaining biofilm in the region adjacent to the cleared zone where the HSC showed ripples had formed. Then we measured the area of a single bacterium ($A = 0.52 \pm 0.09$ μm^2, $n = 6$) and, using the threshold function, we measured the biofilm area coverage. To estimate the density of cells, we divided the area of the biofilm by the area of a cell and divided this again by the area of the ROI (452.8 μm^2) to give cells per surface area. For comparison, the cell-density was also measured from confocal images in peripheral regions of the slide unaffected by the air jet.

Scanning electron microscopy

SEM (FEI Quanta-200) was used to qualitatively assess the structures of the biofilms of the three species in high resolution. Biofilm slides were processed by first immersing in 200 μl of fixative solution (3% glutaraldehyde, 0.1 M sodium cacodylate and 0.15% alcian blue). After 1 h of incubation in the fridge the samples were washed with 0.1 M sodium cacodylate and incubated for 1 h at room temperature. Next, the samples were incubated for 1 h with 200 μl of secondary fixative solution (0.1 M osmium tetroxide and 0.1 M sodium cacodylate). The solution was then replaced with 0.1 M sodium cacodylate and the samples were incubated for 1 h at room temperature. Finally, the samples were placed though an ethanol series (30, 50, 70, 95 and (two times) 100%), adding and replacing 1 ml of each concentration. All the concentrations were incubated at room temperature for 15 min, except for 100% which was incubated for 20 min. After processing, the samples were critical point dried and then sputter coated with gold.

Mathematical model

The system being studied is sketched in Supporting Information Fig. S1. The top fluid (air) is moving initially horizontally with velocity $\overrightarrow{u_a}$ while the bottom fluid (biofilm) is initially stationary. We assume that the dynamics of the air layer can be described using Euler equations:

$$\frac{\partial \overrightarrow{u_a}}{\partial t} + \overrightarrow{u_a} \cdot \nabla \overrightarrow{u_a} = -\frac{1}{\rho_a} \nabla p_a, \tag{9}$$

$$\nabla \cdot \overrightarrow{u_a} = 0. \tag{10}$$

where the velocity is denoted $\overrightarrow{u_a}$, the pressure in the upper layer is denoted p_a and the air density is denoted ρ_a. To reflect the biofilm structure, we modelled the second fluid using a widely accepted model for the biofilm material referred to as a multiphase model that assumes that the biofilm is composed of both fluid and solid components (e.g., encapsulated water and EPS/bacterial components) (Cogan and Keener, 2004; Klapper and Dockery, 2006; Winstanley *et al.*, 2010; Seminara *et al.*, 2012).The underlying assumption is that any infinitesimal volume of the biofilm can be separated into solid, occupying a fraction of the volume θ_s. Since the biofilm consists entirely of either solid or fluid, the fluid volume fraction (θ_f) and the solid volume fraction must sum to one. Therefore, $\theta_f = 1 - \theta_s$. We also assume that the solid and liquid components of the biofilm have the same density, allowing us to neglect buoyancy forces within the biofilm. This also implies that conservation of mass is equivalent to conservation of volume fraction. The governing dynamical equations are derived from conservation of mass/volume and momentum, where the latter assumes that the biofilm material is in force balance. The equations of motion are:

$$\frac{\partial \theta_f}{\partial t} + \nabla \cdot \left(\theta_f \nabla \overrightarrow{u_f}\right) = 0, \tag{11}$$

$$\frac{\partial \theta_s}{\partial t} + \nabla \cdot \left(\theta_s \nabla \overrightarrow{u_s}\right) = 0, \tag{12}$$

$$\mu_f \nabla \cdot (\theta_f \nabla \overrightarrow{u_f}) + \frac{1}{\rho_f} \theta_f \nabla p + \xi \theta_f \theta_s \left(\overrightarrow{u_f} - \overrightarrow{u_s}\right) = 0, \tag{13}$$

$$\mu_s \nabla \cdot (\theta_s \nabla \overrightarrow{u_s}) + \frac{1}{\rho_s} \theta_s \nabla p - \xi \theta_f \theta_s \left(\overrightarrow{u_f} - \overrightarrow{u_s}\right) = 0, \tag{14}$$

$$\theta_s - \theta_f = 1, \tag{15}$$

We used the standard Bernoulli matching condition that incorporates surface tension that arises between the materials (Funada and Joseph, 2001). Then, we carried out linear stability analysis for the two-fluid model of a biofilm by perturbing the interface that separates the two materials (See Supporting Information Materials and Methods). As the shear forces drag the biofilm, certain wavelengths grow while the growth of others are suppressed by surface tension and other forces. We used a baseline biofilm viscosity (η) of 2.8×10^5 Pa.s, which was the mean η measured on similar *S. mutans* biofilms (Vinogradov *et al.*, 2004). We also performed the analysis using values of 1/10th and 10$\times$ the baseline value.

Statistical analysis

Data were analysed by analysis of variance (One-way ANOVA) followed by the Tukey–Kramer multiple comparisons test.

Acknowledgements

This work was financially funded in part by EPSRC DTP EP/K503130/1 award and in part by Philips Oral Healthcare, Bothell, WA, USA. N.G. Cogan was supported in part by NSF CBET 1510743. The authors acknowledge Dr. Janice M. Barton and Dr. Marco Longana from the Testing and Structures Research Laboratory (TSRL, University of Southampton, UK) for providing the HSC setup. They would like to thank Dr. David Johnston and the Southampton Biomedical Imaging Unit for their support in imaging the biofilms. They also gratefully acknowledge the helpful suggestions and comments on fluid dynamics of Dr. Davide Lasagna from the Engineering and the Environment department at the University of Southampton (UK). All data supporting this study are openly available from the university of Southampton repository at https://doi.org/10.5258/SOTON/387042. MS and MW are employed by Philips Oral Healthcare, Bothell, WA, USA. AR, MJ and BG are employed by Philips Research Eindhoven, Netherlands. PS has served as a private consultant for POH. The other authors declare no potential conflicts of interest with respect to the authorship and/or publication of this article.

References

Asali, J., and Hanratty, T. (1993) Ripples generated on a liquid film at high gas velocities. *Int J Multiph Flow* **19:** 229–243.

Battin, T.J., Kaplan, L.A., Newbold, J.D., Cheng, X., and Hansen, C. (2003) Effects of current velocity on the nascent architecture of stream microbial biofilms. *Appl Environ Microbiol* **69:** 5443–5452.

Billings, N., Birjiniuk, A., Samad, T.S., Doyle, P.S., and Ribbeck, K. (2015) Material properties of biofilms – a review of methods for understanding permeability and mechanics. *Rep Prog Phys* **78:** 036601.

Blauert, F., Horn, H., and Wagner, M. (2015) Time – resolved biofilm deformation measurements using optical coherence tomography. *Biotechnol Bioeng* **112:** 1893–1905.

Böl, M., Möhle, R.B., Haesner, M., Neu, T.R., Horn, H., and Krull, R. (2009) 3D finite element model of biofilm detachment using real biofilm structures from CLSM data. *Biotechnol Bioeng* **103:** 177–186.

Cense, A., Peeters, E., Gottenbos, B., Baaijens, F., Nuijs, A., and Van Dongen, M. (2006) Mechanical properties and failure of *Streptococcus mutans* biofilms, studied using a microindentation device. *J Microbiol Methods* **67:** 463–472.

Chen, Z., Chen, X., and Chen, J. (1997) Effects of an oscillating interface on heat transfer. *Chem Eng Sci* **52:** 3265–3275.

Cogan, N. (2010) An extension of the boundary integral method applied to periodic disinfection of a dynamic biofilm. *SIAM J Appl Math* **70:** 2281–2307.

Cogan, N., and Keener, J.P. (2004) The role of the biofilm matrix in structural development. *Math Med Biol* **21:** 147–166.

Cohen, L.S., and Hanratty, T.J. (1965) Generation of waves in the concurrent flow of air and a liquid. *AIChE J* **11:** 138–144.

Costerton, J.W., Stewart, P.S., and Greenberg, E. (1999) Bacterial biofilms: a common cause of persistent infections. *Science* **284:** 1318–1322.

Craik, A.D. (1966) Wind-generated waves in thin liquid films. *J Fluid Mech* **26:** 369–392.

De Leenheer, P., and Cogan, N. (2009) Failure of antibiotic treatment in microbial populations. *J Math Biol* **59:** 563–579.

Drescher, K., Shen, Y., Bassler, B.L., and Stone, H.A. (2013) Biofilm streamers cause catastrophic disruption of flow with consequences for environmental and medical systems. *Proc Natl Acad Sci USA* **110:** 4345–4350.

Fabbri, S., and Stoodley, P. (2016) Mechanical properties of biofilms. In *The Perfect Slime: Microbial Extracellular Polymeric Substances (EPS)*. Flemming, H.-C., Neu, T.R., and Wingender, J. (eds). IWA Publishing, London, UK, pp. 153–172.

Fabbri, S., Johnston, D.A., Rmaile, A., Gottenbos, B., De Jager, M., Aspiras, M., *et al*. (2015) *Streptococcus mutans* biofilm transient viscoelastic fluid behaviour during high-velocity microsprays. *J Mech Behav Biomed Mater* **59:** 197–206.

Fabbri, S., Johnston, D., Rmaile, A., Gottenbos, B., De Jager, M., Aspiras, M., *et al*. (2016) High-velocity microsprays enhance antimicrobial activity in *S. mutans* biofilms. *J Dent Res* **95:** 1494–1500.

Fassel, T.A., and Edmiston, C.E. (1999) Bacterial biofilms: strategies for preparing glycocalyx for electron microscopy. *Methods Enzymol* **310:** 194–203.

Flemming, H.C. (2016) Dark matter of biofilms. In *The Perfect Slime: Microbial Extracellular Polymeric Substances (EPS)*. IWA (International Water Assn), London, UK, pp. 1–23.

Flemming, H.-C., and Wingender, J. (2010) The biofilm matrix. *Nat Rev Microbiol* **8:** 623–633.

Friedman, A. (2015) Free boundary problems in biology. *Philos Trans R Soc A* **373:** 20140368.

Funada, T., and Joseph, D. (2001) Viscous potential flow analysis of Kelvin–Helmholtz instability in a channel. *J Fluid Mech* **445:** 263–283.

Geyer, W.R., Lavery, A.C., Scully, M.E., and Trowbridge, J.H. (2010) Mixing by shear instability at high Reynolds number. *Geophys Res Lett* **37:** 22.

Hanks, R.W., and Ruo, H.C. (1966) Laminar-turbulent transition in ducts of rectangular cross section. *Ind Eng Chem Fundam* **5:** 558–561.

Inglis, T. (1993) Evidence for dynamic phenomena in residual tracheal tube biofilm. *Br J Anaesth* **70:** 22–24.

Joseph, D.D., and Renardy, Y. (2013) *Fundamentals of Two-Fluid Dynamics: Part I: Mathematical Theory and Applications*. Springer Science & Business Media, Springer-Verlag, New York.

Klapper, I., and Dockery, J. (2006) Role of cohesion in the material description of biofilms. *Phys Rev E* **74:** 031902.

Klapper, I., Rupp, C.J., Cargo, R., Purvedorj, B., and Stoodley, P. (2002) Viscoelastic fluid description of bacterial biofilm material properties. *Biotechnol Bioeng* **80:** 289–296.

Lappin-Scott, H.M., and Costerton, J.W. (1989) Bacterial biofilms and surface fouling. *Biofouling* **1:** 323–342.

Loesche, W.J. (1986) Role of *Streptococcus mutans* in human dental decay. *Microbiol Rev* **50:** 353–380.

Marsh, P.D. (2004) Dental plaque as a microbial biofilm. *Caries Res* **38:** 204–211.

Matsuoka, C. (2014) Kelvin-Helmholtz instability and roll-up. *Scholarpedia* **9:** 11821.

Miles, J.W. (1959) On the generation of surface waves by shear flows Part 3. Kelvin-Helmholtz instability. *J Fluid Mech* **6:** 583–598.

Noffke, N., Gerdes, G., Klenke, T., and Krumbein, W.E. (2001) Microbially induced sedimentary structures: a new category within the classification of primary sedimentary structures. *J Sediment Res* **71:** 649–656.

Noffke, N., Decho, A.W., and Stoodley, P. (2013) Slime through time: the fossil record of prokaryote evolution. *Palaios* **28:** 1–5.

von Ohle, C., Gieseke, A., Nistico, L., Decker, E.M., deBeer, D., and Stoodley, P. (2010) Real-time microsensor measurement of local metabolic activities in ex vivo dental biofilms exposed to sucrose and treated with chlorhexidine. *Appl Environ Microbiol* **76:** 2326–2334.

Peterson, B.W., He, Y., Ren, Y., Zerdoum, A., Libera, M.R., Sharma, P.K., *et al*. (2015) Viscoelasticity of biofilms and their recalcitrance to mechanical and chemical challenges. *FEMS Microbiol Rev* **39:** 234–245.

Picioreanu, C., Van Loosdrecht, M.C., and Heijnen, J.J. (2001) Two-dimensional model of biofilm detachment caused by internal stress from liquid flow. *Biotechnol Bioeng* **72:** 205–218.

Porada, H., Ghergut, J., and Bouougri, E.H. (2008) Kinneyia-type wrinkle structures – critical review and model of formation. *Palaios* **23:** 65–77.

Purevdorj, B., Costerton, J.W., and Stoodley, P. (2002) Influence of hydrodynamics and cell signaling on the structure and behavior of *Pseudomonas aeruginosa* biofilms. *Appl Environ Microbiol* **68:** 4457–4464.

Rmaile, A., Carugo, D., Capretto, L., Zhang, X., Wharton, J.A., Thurner, P.J., *et al*. (2013) Microbial tribology and disruption of dental plaque bacterial biofilms. *Wear* **306:** 276–284.

Rmaile, A., Carugo, D., Capretto, L., Aspiras, M., De Jager, M., Ward, M., and Stoodley, P. (2014) Removal of interproximal dental biofilms by high-velocity water microdrops. *J Dent Res* **93:** 68–73.

Rmaile, A., Carugo, D., Capretto, L., Wharton, J.A., Thurner, P.J., Aspiras, M., *et al*. (2015) An experimental and computational study of the hydrodynamics of high-velocity water microdrops for interproximal tooth cleaning. *J Mech Behav Biomed Mater* **46:** 148–157.

Rupp, C.J., Fux, C.A., and Stoodley, P. (2005) Viscoelasticity of *Staphylococcus aureus* biofilms in response to fluid shear allows resistance to detachment and facilitates rolling migration. *Appl Environ Microbiol* **71:** 2175–2178.

Rusconi, R., Lecuyer, S., Guglielmini, L., and Stone, H.A. (2010) Laminar flow around corners triggers the formation of biofilm streamers. *J R Soc Interface* **7:** 1293–1299.

Schindelin, J., Arganda-Carreras, I., Frise, E., Kaynig, V., Longair, M., Pietzsch, T., *et al*. (2012) Fiji: an open-source platform for biological-image analysis. *Nat Methods* **9:** 676–682.

Schultz, M., Bendick, J., Holm, E., and Hertel, W. (2011) Economic impact of biofouling on a naval surface ship. *Biofouling* **27:** 87–98.

Seminara, A., Angelini, T.E., Wilking, J.N., Vlamakis, H., Ebrahim, S., Kolter, R., *et al*. (2012) Osmotic spreading of *Bacillus subtilis* biofilms driven by an extracellular matrix. *Proc Natl Acad Sci USA* **109:** 1116–1121.

Stewart, P.S. (2014) Biophysics of biofilm infection. *Pathog Dis* **70:** 212–218.

Stoodley, P., Lewandowski, Z., Boyle, J.D., and Lappin-Scott, H.M. (1999a) Structural deformation of bacterial biofilms caused by short-term fluctuations in fluid shear: an in situ investigation of biofilm rheology. *Biotechnol Bioeng* **65:** 83–92.

Stoodley, P., Lewandowski, Z., Boyle, J.D., and Lappin-Scott, H.M. (1999b) The formation of migratory ripples in a mixed species bacterial biofilm growing in turbulent flow. *Environ Microbiol* **1:** 447–455.

Stoodley, P., Boyle, J., Cunningham, A.B., Dodds, I., Lappin-Scott, H.M., and Lewandowski, Z. (1999c) Biofilm structure and influence on biofouling under laminar and turbulent flows. In *Biofilms in the Aquatic Environment*. Keevil, C.W., Godfree, A., Holt, D., and Dow, C. (eds.). The Royal Society of Chemistry Press, Cambridge, pp. 13–24.

Stoodley, P., Sauer, K., Davies, D.G., and Costerton, J.W. (2002a) Biofilms as complex differentiated communities. *Annu Rev Microbiol* **56:** 187–209.

Stoodley, P., Cargo, R., Rupp, C.J., Wilson, S., and Klapper, I. (2002b) Biofilm material properties as related to shear-induced deformation and detachment phenomena. *J Ind Microbiol Biotechnol* **29:** 361–367.

Tauber, W., Unverdi, S.O., and Tryggvason, G. (2002) The nonlinear behavior of a sheared immiscible fluid interface. *Phys Fluids (1994-Present)* **14:** 2871–2885.

Thomas, K., Herminghaus, S., Porada, H., and Goehring, L. (2013) Formation of Kinneyia via shear-induced instabilities in microbial mats. *Philos Trans R Soc A Math Phys Eng Sci* **371:** 20120362.

Trejo, M., Douarche, C., Bailleux, V., Poulard, C., Mariot, S., Regeard, C., and Raspaud, E. (2013) Elasticity and wrinkled morphology *of Bacillus subtilis* pellicles. *Proc Natl Acad Sci USA* **110:** 2011–2016.

Vazquez-Una, G., Chenlo-Romero, F., Sanchez-Barral, M., and Perez-Munuzuri, V. (2000) Mass transfer enhancement due to surface wave formation at a horizontal gas–liquid interface. *Chem Eng Sci* **55:** 5851–5856.

Vinogradov, A.M., Winston, M., Rupp, C.J., and Stoodley, P. (2004) Rheology of biofilms formed from the dental plaque pathogen *Streptococcus mutans*. *Biofilms* **1:** 49–56.

Wilking, J.N., Angelini, T.E., Seminara, A., Brenner, M.P., and Weitz, D.A. (2011) Biofilms as complex fluids. *MRS Bull* **36:** 385–391.

Winstanley, H.F., Chapwanya, M., McGuinness, M.J., and Fowler, A.C. (2010) A polymer – solvent model of biofilm growth. Proc R Soc A. **467**: 1449–1467.

Supporting information

Additional Supporting Information may be found in the online version of this article at the publisher's web-site:

Fig. S1. Power spectra of ripples patterns generated from FFT analysis after *S. mutans* biofilm exposure to air jets at 24.6 m/s (a), 44.9 m/s (b), 68.1 m/s (c), 85.5 m/s (d) and 110.1 m/s (e). The peaks in a FFT spectrum represent periodicities in the data. In this case, the periodicity is the distance between the ripples (i.e., wavelength). Black arrows indicate the position of the peak frequency relative to the wavelength measured experimentally.

Fig. S2. Schematic of the mathematical domain. The top fluid (air) is moving initially horizontally with velocity $\overrightarrow{u_a}$ while the bottom fluid (biofilm) is initially stationary.

Fig. S3. Representative sketch of the dispersion curve that relates the perturbation wavelength, k, and the growth rate, ω of the perturbation.

Fig. S4. Schematic representation of the air jet entry geometry in the IP space. The air compressor nozzle (a) was positioned in the middle of the IP channel created by two microscope glass slides (b). The calculated area of the entry geometry is shown in yellow.

Fig. S5. Schematic showing how the ripple width, wavelength and velocity are measured from successive frames from a high-speed movie. (a) Five consecutive frames from a HSC video showing three biofilm ripples (green crescents) moving along the glass slide (light blue). The middle ripple has been highlighted to show how it would appear as a dark line in the reslice time-trace. A line was traced along three or more well defined ripples (red dashed line) to measure ripples wavelength, width and velocity. (b) Representation of a plot profile graph showing the grey scale values (pi) of the image along the traced line as a function of the length (X). The distance between two consecutive reverse peaks was defined as λ_R and the width of one peak as w_R. (c) Representation of a reslice function graph showing the time-traces along the traced line formed by the moving ripples. The slope of the line was defined as u_R.

Table S1. Parameters used in the mathematical analysis. [a] Fitting, [b] Assumed, [c] Reference (Vinogradov et al., 2004).

Video S1. High-speed camera video of three day old *S. mutans* biofilm colonized slide exposed to a high-velocity water microspray showing ripples structures forming at the biofilm/fluid interface. The nozzle tip was located at the left edge of the slide. Flow was left to right. Scale bar=5 mm.

Video S2. High-speed camera video of three day old *S. mutans* biofilm colonized slide exposed to a high-velocity air microspray showing ripples structures forming at the biofilm/fluid interface. The nozzle tip was located at the left edge of the slide. Flow was left to right. Scale bar=5 mm.

Video S3. High-speed camera video of three days old *S. mutans* biofilm colonized slide exposed to a high-velocity air microspray showing biofilm recoil after the micro spray has ended. The nozzle tip was located at the left edge of the slide. Flow was left to right. Scale bar=2 mm.

Video S4. High-speed camera video of three days old *S. mutans* biofilm colonized slide exposed to a compressed air jet of velocity=24.6 m/s showing ripples structures forming at the biofilm/fluid interface. The nozzle tip was located at the left edge of the slide. Flow was left to right. Scale bar=5 mm.

Video S5. High-speed camera video of three days old *S. mutans* biofilm colonized slide exposed to a compressed air jet of velocity=44.9 m/s showing ripples structures forming at the biofilm/fluid interface. The nozzle tip was located at the left edge of the slide. Flow was left to right. Scale bar=5 mm.

Video S6. High-speed camera video of three days old *S. mutans* biofilm colonized slide exposed to a compressed air jet of velocity=68.1 m/s showing ripples structures forming at the biofilm/fluid interface. The nozzle tip was located at the left edge of the slide. Flow was left to right. Scale bar=5 mm.

Video S7. High-speed camera video of three days old *S. mutans* biofilm colonized slide exposed to a compressed air jet of velocity=85.5 m/s showing ripples structures forming at the biofilm/fluid

Video S8. High-speed camera video of three days old *S. mutans* biofilm colonized slide exposed to a compressed air jet of velocity=110.1 m/s showing ripples structures forming at the biofilm/fluid interface. The nozzle tip was located at the left edge of the slide. Flow was left to right. Scale bar=5 mm

Video S9. High-speed camera video of three days old *S. epidermis* biofilm colonized slide exposed to a compressed air jet of velocity=85.5 m/s showing ripples structures forming at the biofilm/fluid interface. The nozzle tip was located at the left edge of the slide. Flow was left to right. Scale bar=2 mm.

Video S10. High-speed camera video of seven days old *P. aeruginosa* biofilm colonized slide exposed to a compressed air jet of velocity=85.5 m/s showing wrinkles structures forming at the biofilm/fluid interface. The nozzle tip was located at the left edge of the slide. Flow was left to right. Scale bar=2 mm.